European Polymer Journal 179 (2022) 111580

Contents lists available at ScienceDirect

European Polymer Journal

journal homepage: www.elsevier.com/locate/europolj

Gentamicin-loaded polyvinyl alcohol/whey protein isolate/hydroxyapatite 3D composite scaffolds with drug delivery capability for bone tissue engineering applications

Tufan Arslan Tut [a,b], Sumeyye Cesur [a,*], Elif Ilhan [a,b], Ali Sahin [c], Onur Samet Yildirim [d], Oguzhan Gunduz [a,e]

[a] Center for Nanotechnology & Biomaterials Application and Research (NBUAM), Marmara University, Turkey
[b] Department of Bioengineering, Faculty of Engineering, Marmara University, Turkey
[c] Department of Biochemistry, School of Medicine/Genetic and Metabolic Diseases Research and Investigation Center, Marmara University, Istanbul, Turkey
[d] Axolotl Biosystems Ltd, Istanbul, Turkey
[e] Department of Metallurgical and Materials Engineering, Faculty of Technology, Marmara University, Turkey

ARTICLE INFO

Keywords:
Bone tissue engineering
3D printing
Drug delivery
Gentamicin
Whey protein isolate
Hydroxyapatite
Polyvinyl alcohol

ABSTRACT

Bone defects caused by diseases such as bone diseases, tumours, and traumas negatively affect the lives of millions of people around the world. Bone tissue engineering offers a new approach to repairing bone defects. Here, a novel bioactive Polyvinyl alcohol (PVA)/ Whey protein isolate (WPI)/ Hydroxyapatite (HA) composite scaffolds with Gentamicin (GEN)-loaded at varying rates were successfully fabricated by 3D printing technology. The strong interaction between PVA, WPI, HA, and GEN were proved with Fourier transform infrared spectroscopy (FT-IR) and X-ray diffraction (XRD). When the scanning electron microscopy (SEM) images of the produced 3D composite scaffolds were evaluated, it can be said that 3D composite scaffolds with the desired porosity and structure for bone tissue engineering applications were obtained. The 3D PVA/WPI/HA/12GEN composite scaffold was fabricated excellently with its 675 μm pore size. Compression tests revealed that the 3D composite scaffold had a compressive strength of 1.28–1.22 MPa and strain of % 12.89–8.70 and thus met the mechanical desirables of human trabecular bone. Moreover, the compressive strength and strain values of the scaffolds were decreased slightly due to adding the GEN drug. According to the Differential scanning calorimetry (DSC) analysis, it was determined that the highly crystalline structure of PVA was disrupted by adding GEN to the composite scaffolds. It was also observed that the addition of GEN to the scaffold did not significantly affect the swelling and degradation behaviour, and the scaffolds degraded by approximately 55% on the 10th day. The scaffolds exhibited a controlled release profile up to 240 and 264 h and were released with the Korsmeyer-Peppas kinetic model according to the highest correlation number. Cell analysis revealed that biocompatible structures were produced, and osteoblasts formed filopodia extensions, resulting in healthy cell attachment. According to these results, 3D GEN-loaded PVA/WPI/HA composite scaffolds may be a promising innovation for bone defect repair in bone tissue engineering applications.

1. Introduction

Bone tissue is the strongest and hardest among the tissues that make up the body. Bone tissue provides support to the body, enables walking, maintains life, and this tissue is also known as calcium storage. Since the amount of calcium in the tissue is high, it has a hard structure. Xu et al. state that the number of operations performed for bone substitutions is >12 million each year, and this number will increase each year [1]. This situation can be overcome by developing different treatment methods for bone tissue.

Bone tissue engineering is a multidisciplinary field that works on bone tissue and is becoming popular today and can be seen as a treatment method shortly [2]. This field aims to replace cells that have been deformed or damaged for any reason in the body with new cells [3]. The new cells to be implanted should be mechanically and chemically similar to the destroyed old cells. In this way, the tissues near the cell to

* Corresponding author.
E-mail address: sumeyye.cesur@marmara.edu.tr (S. Cesur).

https://doi.org/10.1016/j.eurpolymj.2022.111580
Received 6 June 2022; Received in revised form 7 September 2022; Accepted 9 September 2022
Available online 15 September 2022

be implanted will recognise the new implant, and cell attachment will take place. One of the methods that contribute to bone tissue engineering studies is the production of tissue scaffolds with a 3D printer (Fig. 1).

3D printing technology is a rapidly developing field. The production of personalised prostheses and implants in the field of health has made 3D printing technology used in this field. In addition, the support of 3D printing technology with computer-aided programs can ensure that the dimensions of the structures to be produced are to the desired specifications [4]. The pore sizes of the tissue scaffolds can be adjusted to be the same as the actual pore size of the bone with computer-aided programs. In this way, a scaffold similar to the structure of the real bone can be produced. In 3D printing technology, it is an essential parameter that the solutions of biofunctional inks are suitable for printing to produce tissue scaffolds. The scaffolds to be produced are among the features expected to be compatible with the body, not cause toxic effects, preserve cell viability, and improve within the expected time [5].

The materials to be used in bioprinting should be biocompatible and should not have a toxic effect on the body. It is also to support and facilitate the functions of the damaged area in the human body and provide structure for cell migration and population. Among these materials, synthetic polymers are often preferred in bone tissue engineering because they can be easily shaped. Polyvinyl alcohol (PVA) is one of the synthetic polymers and has water-soluble properties and high biocompatibility. Xu et al. showed that PVA polymer could be used in bone tissue engineering applications by combining it with β-tricalcium phosphate and dipyridamole drug [6]. In addition, PVA has high mechanical properties. Because of this feature, the design of PVA-based nanocomposites to provide bone regeneration has been investigated by researchers in previous studies [7]. The inclusion of bioceramics, particularly hydroxyapatite (HA), can increase the bioactivity of PVA-based nanocomposite scaffolds [8].

Hydroxyapatite (HA) is a calcium phosphate compound. It is a medical bioceramic material that makes up about 70% of the weight of the human bone [9]. Due to its excellent osteoconductivity, good biocompatibility, and chemical similarity to natural bone, it is

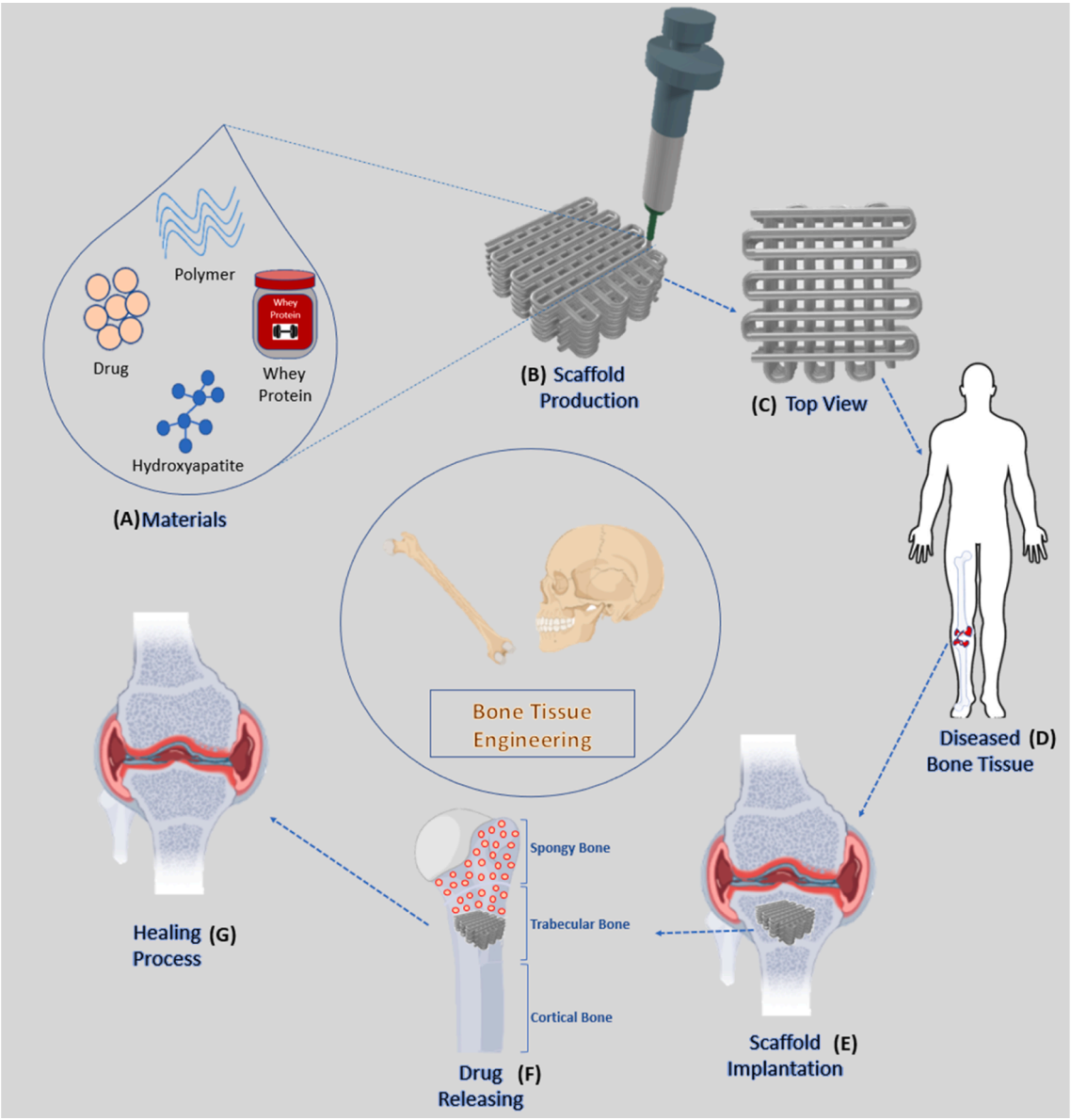

Fig. 1. (A) Required materials for producing scaffolds. (B) Scaffold production process with a 3D printer. (C) Top view of the produced scaffolding. (D) Diseased bone tissue that is aimed to be replaced with new tissue. (E) Implantation of the scaffold in the body. (F) Drug releasing process of the implanted scaffold. (G) The healing process of the bone tissue.

considered one of the most suitable materials for producing bone scaffolds [10]. Due to its osteoconductive properties and high bioactivity, HA has become an important material for tissue engineering applications, especially as a filler in the bone regeneration [11,12]. Bendtsen et al. combined PVA and hydroxyapatite to produce scaffolds with a 3D printer for the bone tissue engineering [13]. In addition, HA is used in many applications such as drug delivery and tooth enamel repair [14].

Whey protein contains 20% of the proteins in milk and has been effective in many medical applications on muscle, bone, pancreas, immunity, cancer, metabolism, ageing, learning, and wound healing. In addition, thanks to the calcium in it, it supports the health of the bones in the future [15]. Whey protein isolate (WPI) has attracted attention as a new material in many applications. For example, it has been used with other materials such as calcium phosphates, bioglasses, or other minerals to produce bone scaffolds [16]. It is an excellent airgel precursor with good mechanical properties that can be used as a drug carrier [17]. In addition, Douglas et al. reported that WPI dissolved in a cell culture medium promotes the proliferation of human neonatal dermal fibroblasts (FIB) and human osteoblast-like Saos-2 cells [18]. This suggests that WPI may be a promising component for the bone tissue regeneration [19].

In addition to all these materials used, gentamicin will be used in the study to increase healing. Gentamicin is a broad-spectrum antibiotic used to treat diseases caused by bacterial infections. It is used to inflammation the heart membrane, pneumonia and bone infections. Gentamicin is on the World Health Organization's List of Essential Medicines due to its high efficiency against gram-negative bacteria and low toxicity [20]. In this study, two different ratios of gentamicin (6 mg/12 mg) will be tried, and it will be observed which drug ratio is more suitable for the healing of cells. Many researchers are working on repairing bone damage using various combinations of scaffolds with several methods. But there is still a need for new combinations. The main novelty of this work is a new combination of 3D printing.

In this study, PVA/WPI/HA, PVA/WPI/HA/6GEN, and PVA/WPI/HA/12GEN composite scaffolds were successfully produced with 3D printing technology. Fabricated scaffolds were characterised by Fourier transform infrared spectroscopy (FT-IR), differential scanning calorimetry (DSC), X-ray diffractometry (XRD), scanning electron microscopy (SEM), compression test, drug release test, swelling and degradation behaviour, and in vitro cell culture assay. This study is promising in bone tissue engineering to design an alternative and innovative bone tissue scaffold to treat bone defects where infection occurs.

2. Materials and methods

2.1. Materials

Polyvinyl alcohol (PVA, MW = 89,000–98,000), glutaraldehyde solution (GA,50 % wt. MW = 100.12 g/mol) and phosphate buffer saline (PBS, pH = 7.4), were purchased from Sigma Aldrich (USA). Whey protein isolate (WPI) was purchased from Alfasol (Turkey). Gentamicin Sulfate (Potency: >590 μg/mg) was obtained from BioShop (Canada). Hydroxyapatite (HA, MW = 502.31 g/mol) was purchased from Oerlikon Metco (Switzerland).

2.2. Preparation and characterisation of solutions

Solutions used for scaffold fabrication were prepared as shown in Table 1. Firstly, 12% PVA was dissolved in 10 ml of distilled water at 120 °C for 45 min on a magnetic stirrer. 1 g of whey protein isolate (WPI) was added to the PVA solution. After the WPI was completely dissolved, 6 mg and 12 mg gentamicin were added to the solutions separately and mixed for 20 min. Finally, 140% hydroxyapatite was added to the solutions and mixed with magnetic stirring. To determine the rheological property of composite scaffold solutions, viscosity was measured by a digital viscometer (RM 200 CP4000 Plus, Lamy Rheology, France).

Table 1
Contents of solutions used in scaffold production.

Solutions	PVA Conc. (wt %)	WPI Conc. (wt %)	HA Conc. (wt %)	GEN Conc. (wt %)
PVA/WPI/HA	12	10	140	–
PVA/WPI/HA/6GEN	12	10	140	0.06
PVA/WPI/HA/12GEN	12	10	140	0.12

Before the tests, the equipment was calibrated, and all samples were tested in triplicate at 60 s^{-1} shear rate and 25 °C room temperature.

2.3. Design and 3D printing of the scaffolds

Scaffolds were designed with SolidWorks®, which is CAD Software. Scaffolds are designed as squares with dimensions of 20 × 20 × 6 mm^3. The designed scaffolds were saved in STL (stereolithography) format so that the 3D printer's interface could recognise the designed object. The designed scaffold in STL format was transferred to the RepetierHost program so that it could be printed with a 3D printer (AXO-A3, Axolotl Biosystems). Since the scaffolds will be produced with the Axolotl Biosystems 3D printer and the 3D printer is integrated into the RepetierHost program, the previously designed scaffolds were transferred to the RepetierHost program. In scaffold production, fill density was set to 26%, and fill angle was 90°. As the fill pattern, rectilinear was chosen. Infill speed was determined as 4 mm/s. The inner diameter of the needle was 0.84 mm. The distance of the needle tip from the printing surface was set to 0.3 mm. The number of layers was determined as 6 for each scaffold. In this way, the height of the scaffolds was 5 mm (Table 2).

2.4. Crosslinking process of the produced scaffolds

Cross-linking of the produced scaffolds (Fig. 2) was carried out using glutaraldehyde vapour. A 25% glutaraldehyde solution was prepared. Scaffolds were exposed to the crosslinking process in the steam of this prepared solution in an oven at 37 °C for 3 h.

2.5. Scanning electron microscopy (SEM)

Scanning electron microscopy (SEM, EVA MA 10, ZEISS) was used to investigate the morphological characterisation of scaffolds. Before starting the examination, the scaffolds were coated with gold–palladium for 180 s using a sputter coater (Quorum SC7620, ABD) to gain conductivity. Also, average pore size was analysed using image software (Olympus AnalySIS, USA).

2.6. Fourier Transform-Infrared spectroscopy (FT-IR) analysis

FTIR is an analytical method used for the chemical characterisation of structures. The presence of chemical bonds and functional groups of the scaffolds was demonstrated by Fourier Transform-Infrared Spectroscopy (Jasco, FT-IR 4700). All spectrums were taken at 400–4000 cm^{-1} scanning range and 4 cm^{-1} resolution.

Table 2
Process parameters of scaffolds during 3D printing.

Parameters	Values
Number of Layers	6
Needle Tip Inner Diameter (mm)	0.84
Room Temperature (°C)	25
Printing Surface Temperature (°C)	25
Infill Density (%)	26
Infill Speed (mm/s)	4

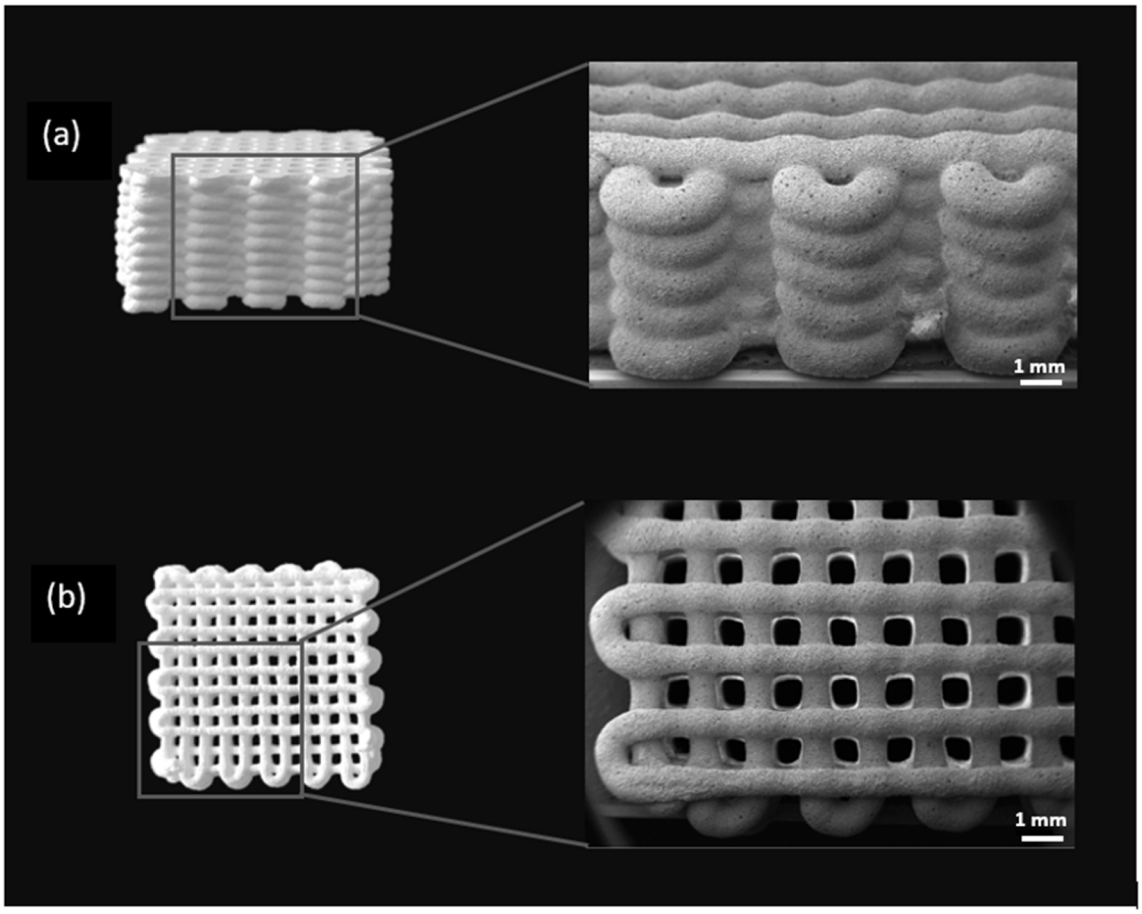

Fig. 2. (a) Side view photo and SEM image, (b) Top view photo and SEM image of 3D printed composite scaffold.

2.7. X-Ray diffraction (XRD)

The structural characterisation of the scaffolds was analysed using the XRD machine (Shimadzu – 6100). Measurements were performed at 40 kV and 30 mA over the 2θ range of 10–90°–60° at 2°/min. OriginPro 7.0 software (OriginLab Corporation, MA, USA) analysed the acquired data.

2.8. Differential scanning calorimetry (DSC)

The thermal properties of the scaffolds were determined using the DSC (Shimadzu DSC-60 Plus) analysis method. Scaffolds were tested in the temperature range of 25–400 °C and at a scanning rate of 10 °C/min.

2.9. Mechanical properties of the scaffolds

The compression test is a mechanical analysis method in which the shortening or crushing of the material is observed as a result of the force applied to the structure. The mechanical strength of the scaffolds was determined using a compression testing machine (SHIMADZU, EZ-LX).

2.10. Swelling and degradation tests of the scaffolds

Swelling and degradation characteristics of scaffolds were demonstrated by swelling and degradation tests. Scaffolds were kept in 1 ml of phosphate buffer saline (PBS, pH = 7.4) containing Eppendorf tubes at 37 °C and 250 revolutions per minute (rpm) in a thermoshaker (BIOSAN TS-100C) for 1–20 days. The swelling test was performed on three samples of each scaffold. For the swelling test, scaffolds in PBS were taken every day, and their mass was measured. Initial weights (Wo) of the scaffolds were measured on the first day. The wet weights (Ww) of the samples were weighed daily for the swelling test. The swelling value (S) was calculated by using Eq. (1) [21].

$$S = \frac{(Ww - Wo)}{Wo} \times 100 \quad (1)$$

For the degradation test, the scaffold in the Eppendorf tube was incubated in PBS for 1 day. After 1 day, all of the PBS in the Eppendorf tube was drained and left to dry in the scaffold oven for 1 day. The weight of the dried scaffold was measured after 1 day. The weight loss (Di) was calculated as in Eq. (2) for the degradation of scaffolds [21].

$$Di = \frac{(Wo - Wt)}{Wo} \times 100 \quad (2)$$

where Wo and Wt are weights of the scaffolds before and after degradation, respectively.

2.11. Encapsulation efficiency and drug release test

In this study, UV–VIS Spectroscopy (Lambda 35, Perkin Elmer, UK) will be used in drug release testing. First of all, gentamicin was prepared at 3 different concentrations (0.25, 0.5, and 1 μg/mL) to create a linear calibration curve, and the absorbance graph was drawn. Drug release testing of scaffolds with gentamicin concentrations of 6 mg (6 GEN) and 12 mg (12 GEN) was performed. The scaffolds were put into Eppendorf tubes, and 1 ml of PBS (pH = 7.4) was added. They were kept in a thermoshaker (BIOSAN TS-100C) at 37 °C and 250 rpm for the specified time intervals. At the end of the determined time intervals, PBS in the Eppendorf tubes was taken with the help of a micropipette and placed in the spectrophotometer cuvette. Its absorbance was measured in the

190–500 nm wavelength. Each scaffold was tested in triplicate. After each measurement, new PBS was added to the Eppendorf tube.

The drug-loaded scaffolds were weighed (approximately 45 mg) and dissolved in 10 ml of their solvent in the beaker under stirring for 1 h to determine the encapsulation efficiency. After stirring for 1 h, 1 ml of the solution was taken, and detection of gentamicin drug in the solution was determined using a UV − visible spectrophotometer at 201 nm. For all scaffolds, this procedure was done in triplicate. Encapsulation efficiency (%) was calculated using Eq. (3) [22].

$$\text{Encapsulation efficiency } \% = \frac{Wt}{Wi} \times 100 \tag{3}$$

where Wt is the actual amount of drug-loaded in the scaffolds and Wi is the amount of drug used in fabricated scaffolds.

The drug release kinetics of the scaffolds were evaluated using different mathematical models such as zero-order(4), first-order(5), Korsmeyer-Peppas(6), Higuchi(7), and Hixson-Crowell(8), and their equations are as follows;

$$Q = K_0 t \tag{4}$$

$$In(1 - Q) = -K_1 t \tag{5}$$

$$Q = Kt^n \tag{6}$$

$$Q = K_h t^{1/2} \tag{7}$$

$$Q^{1/3} = K_{hc} t \tag{8}$$

In these equations, Q is the fractional amount of drug release at time t; K, K_0, K_1, K_h, and K_{hc} are the kinetic constants for Korsmeyer-Peppas, zero-order, first-order, Higuchi, and Hixson-Crowell models, respectively. n is the diffusion exponent, which is indicative of the drug release mechanism.

2.12. Cell culture test for scaffolds

Circular scaffolds (1.6 mm thick and 12 mm in diameter) produced with a 3D printer were placed in 12-well plates and sterilised by exposure to ultraviolet (UV) light overnight. The scaffolds were incubated in a cell culture medium for 2 h before seeding. To examine cell adhesion and viability, Human osteoblast cells (ATCC) suspension was seed planted on the scaffold at 37 °C and 5% CO_2. To analyse cell viability, the 3-(4,5-Dimethylthiazol-2-yl)-2,5-Diphenyltetrazolium Bromide) MTT test was applied to the scaffolds after 1, 3, and 7 days of incubation according to manufacturer's protocol. The absorbance value of cytotoxicity test was measured at 570 nm wavelength (690 nm as Ref. value) in ELISA reader (Enspire, Perkin Elmer). The assay was studied 3 times and average of results was considered as final result. Before the MTT test took place, the scaffolds were washed with cold PBS (pH 7.4), and then 0.5 mg/ml (0.5 ml) of MTT solution was added and incubated for 5 h at 37 °C with 5% CO_2. The supernatant was drained gently from the solution, and then 1.5 ml of dimethylsulfoxide (DMSO) was added. Plates were again incubated for 15 min at 37 °C under 5% CO_2 condition and with a microplate reader at 560 nm wavelength absorbance was measured. Morphological analyses of fixed osteoblasts on scaffolds were performed using scanning electron microscopy (SEM, Zeiss EVO MA-10). After 1,3 and 7 days of incubation of scaffolds, scaffolds were fixed with 2.5% glutaraldehyde (Sigma) for 2 h and with serial dilutions of ethanol (30%, 50%, 70%, 90%, and 99%) were dried. The dried scaffolds were gold-coated with sputter-coated (Quorum Technologies, SC 7620) for 90 s and observed by SEM (Zeiss, EVO MA-10) at 10 kV voltage.

3. Result & discussion

3.1. Characterization of rheological properties of solutions

In 3D-bioprinting, the physical properties of biofunctional inks play an essential role in producing composite structures. Viscosity is an important parameter for the production of scaffolds by the 3D bioprinting method. The viscosity of the prepared solution should be suitable for printability with a 3D printer [23]. As a result of the viscosity measurement, it was determined that the PVA/WPI/HA solution had the lowest viscosity value (686,000 mPa.s), then PVA/WPI/HA/6GEN had the viscosity value (720,900 mPa.s) and PVA/WPI/HA/12GEN solution had the highest viscosity value (722,000 mPa.s). This shows that the addition of GEN to the scaffolds effectively increases the viscosity. There is also a close relationship between the viscosity and the pore size of the scaffolds [23].

3.2. Morphological characterization of scaffolds

When the SEM images in Fig. 3(b) are examined, it is seen that the scaffold without GEN has a pore size of 748.36 ± 67.50 μm. However, Fig. 3(d) shows that the GEN-loaded scaffold has a pore size of 675.55 ± 60.71 μm. The increase in viscosity with the addition of GEN caused a decrease in pore size. Other studies have shown that the low viscosity of biofunctional ink causes the solution to tend to spread during printing, resulting in the collapse of the top layers of scaffold [24]. As a result of the viscosity measurement made in this study, the addition of GEN resulted in both an increase in viscosity and a decrease in pore size. It has been reported that high viscosity causes uneven scaffold structure and printability problems in the 3D bioprinting [25]. However, in this study, the increase in viscosity did not cause any negative effects in terms of printability with 3D printers and performed the characterization tests of composite structures.

The porous structure of tissue scaffolds is necessary for gas permeability and cell nutrition, and the optimal pore size may vary depending on the type of tissue [26]. SEM images of 3D-printed scaffolds are shown in Fig. 3. It was observed that all of the produced composites had a single distribution and the pores had a square shape. The mean pore size value of the non-crosslinked composite shown in Fig. 3(a) was 748.36 ± 67.50 μm. The average pore size value of the crosslinked composite shown in Fig. 3(b) was 716.25 ± 101.17 μm. The average pore size of the crosslinked composite is smaller than that of the non-crosslinked composite. That is, as a result of the crosslinking process, it is seen that the pore size of the structure has decreased compared to the initial situation. This is because the crosslinking process makes the structure more rigid [27]. The mean pore sizes of the PVA/WPI/HA/6GEN and PVA/WPI/HA/12GEN composites were shown in Fig. 3(c, d) as 678.61 ± 66.37 μm and 675.55 ± 60.71 μm, respectively. It was observed that the pore size of the scaffolds decreased with the loading of gentamicin drug on the produced PVA/WPI/HA tissue scaffolds. In the study by Morawska et al., it was reported that loading the scaffolds with drugs caused a decrease in the pore size [28]. When the SEM images of the scaffolds in Fig. 3(a, b, c, d) are examined, it is seen that they have rough surfaces. It is thought that the spherical particles seen on the surface of the scaffolds originate from the HA spherical powders used in the production of composites [29]. In bone tissue engineering applications, it has been seen that cellular growth and bone ingrowth are provided with a pore size between 100 and 1000 μm [30]. It can be said that the fabricated scaffolds have a suitable range of pore size values to provide cellular growth and bone ingrowth for bone tissue engineering applications.

3.3. Fourier transform infrared spectroscopy (FT-IR)

Chemical structures and functional groups of pure materials and their composites were determined by FTIR spectroscopy. In Fig. 4 (A, a), WPI absorption peaks are seen. The peak at ~3272.6 cm^{-1} is due to

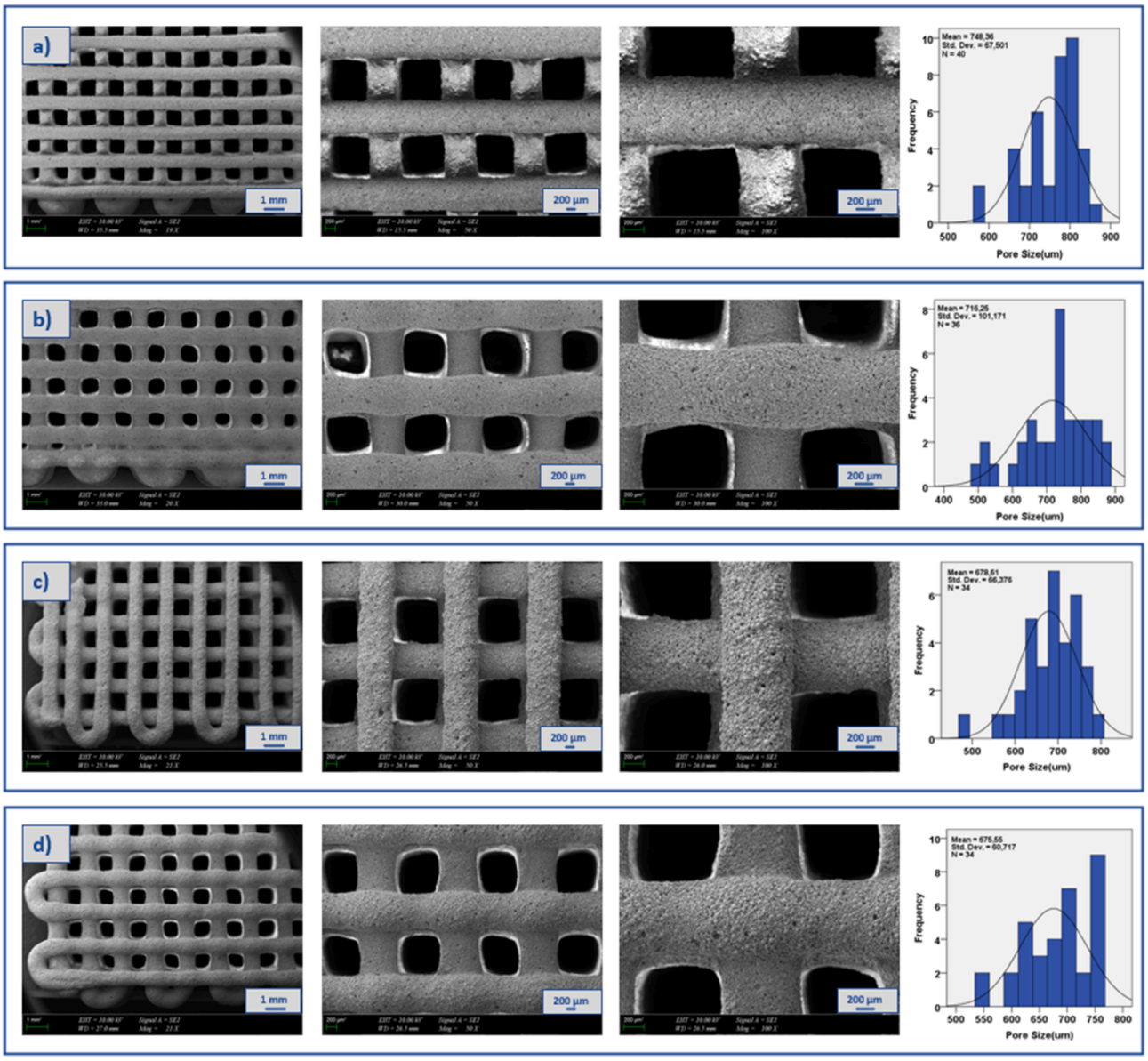

Fig. 3. SEM images of the Non-crosslinked PVA/WPI/HA (a), Crosslinked PVA/WPI/HA (b), PVA/WPI/HA/6GEN (c), PVA/WPI/HA/12GEN (d).

stretching vibrations of –OH linked to $–NH_2$. The peak at ~2925.5 cm^{-1} is related to the $–CH_2$ group. The peak at ~1627.6 cm^{-1} ($–CO\text{-}NH_2$) is a characteristic band of the primary amide group of proteins. The peak, which is seen at ~1525.4 cm^{-1} (–CO-NH), is the secondary amide group of proteins. The peak at ~1045.2 cm^{-1} indicates the -C-OH group [31]. In Fig. 4 (A, b), the peaks of GEN are seen. The peak at ~2881.1 cm^{-1} shows the (C–H) group due to alkyl stretching vibrations of GEN. At the peak, ~1617.9 cm^{-1}, amide bending vibrations of the primary aromatic amines (N–H) group can be seen. The peak at ~1525.42 cm^{-1} corresponds to C–H stretching vibrations. The peak, which is seen at ~1031.73 cm^{-1}, corresponds to the S–O stretch [32,33]. Fig. 4(A, c) shows the peaks of PVA. O–H stretching is observed due to intramolecular and intermolecular hydrogen bonds at ~3271.6 cm^{-1}. C–H stretching of the alkyl groups is observed at the peak at ~2909.1 cm^{-1}. C=O carbonyl stretch is seen at ~1712.4 cm^{-1}. C–H bending vibration of CH_2 is visible on the peak at ~1425.1 cm^{-1}. C–H deformation vibration is seen on the peak at ~1239.1 cm^{-1} [34,35]. In Fig. 4 (A, d), absorption peaks for HA are shown. The HA peaks are at ~1087.6 cm^{-1}, ~1016.3 cm^{-1}, ~962.3 cm^{-1}, ~628.6 cm^{-1}, and ~561.1 cm^{-1} are associated with PO_4^{-3} asymmetric stretching, PO_4^{-3} asymmetric stretching, PO_4^{-3} symmetric stretching, OH bending and asymmetric bend of PO_4^{-3}, respectively [36,37]. In Fig. 4 (A, e), (A, f), (A, g), the absorption peaks of the composites which are formed by the combination of pure materials are observed. It was observed that all of the composites in Fig. 4 (A, e), (A, f), (A, g) were given peaks at the same peak points ~ 1087.6 cm^{-1}, ~962.3 cm^{-1}, and ~561.1 cm^{-1} with the pure HA, which is shown in Fig. 4 (A, d). This is because the same amount of HA is used to produce pure, 6 mg, and 12 mg composites. The other reason is that HA is used in a higher amount than other materials (PVA, WPI, and GEN) in composites production. When the peak of GEN observed in Fig. 4(A, b) at ~1031.73 cm^{-1} was compared to the peaks of the composites, the transmittance was lower at this peak in the pure composite (without GEN drug) in Fig. 4 (A, e). Therefore, the curve of the pure composite is less sharp at this peak. The transmittance of the composite, which contains 6 mg of GEN in Fig. 4 (A, f), was higher than the pure composite. Accordingly, the curve of this composite is sharper at this peak than the pure composite. In the 12 mg GEN-containing composite in Fig. 4 (A, g), the transmittance at this peak was higher than the other two composites (pure and 6 mg GEN). It was observed that the curve of this composite was sharper than the other two

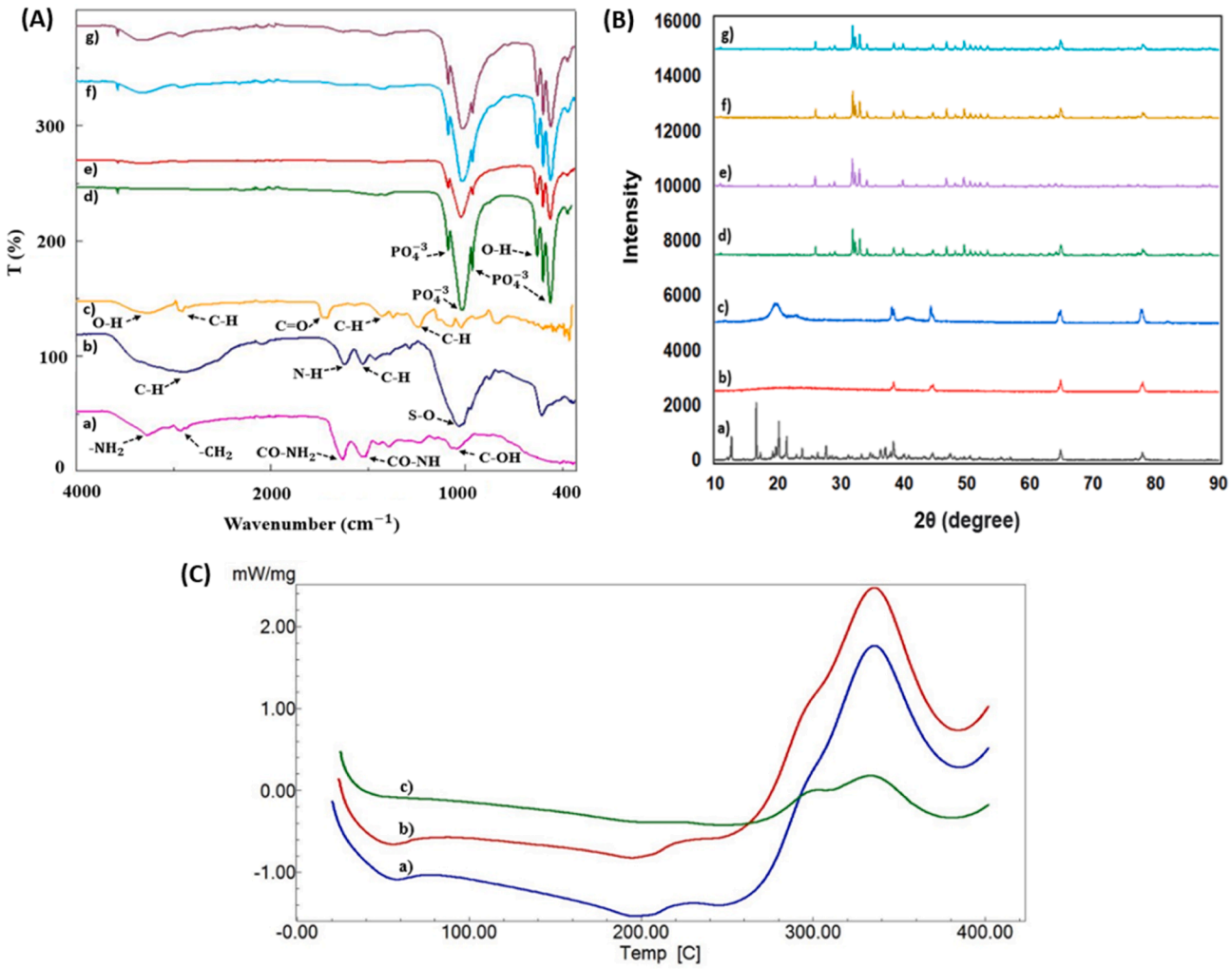

Fig. 4. FTIR spectrums of (A,a) WPI, (A,b) GEN, (A,c) PVA, (A,d) HA, (A,e) PVA/WPI/HA, (A,f) PVA/WPI/HA/6GEN, (A,g) PVA/WPI/HA/12GEN. XRD spectra of (B, a) WPI, (B,b) GEN, (B,c) PVA, (B,d) HA, (B,e) PVA/WPI/HA, (B,f) PVA/WPI/HA/6GEN, (B,g) PVA/WPI/HA/12GEN. DSC thermogram of (C,a) PVA/WPI/HA, (C,b) PVA/WPI/HA/6GEN, (C,c) PVA/WPI/HA/12GEN.

composites (pure and 6 mg GEN). This showed that the S–O stretch at this peak in GEN is more easily seen in drug-loaded composites (6 mg, 12 mg) as the drug increases.

3.4. X-ray diffraction analysis (XRD)

X-ray diffraction results of WPI, GEN, PVA, HA, PVA/WPI/HA, PVA/WPI/HA/6GEN, and PVA/WPI/HA/12GEN samples were shown in Fig. 4 (B). Sharp diffraction peaks in XRD spectra indicate crystalline fractions [38]. The XRD spectrum of WPI (Fig. 4 (B, a)) exhibited sharp peaks at 2θ of 12.6° and 21.34°. The peaks at these degrees indicate that WPI has a good crystallinity degree, and therefore, WPI has a semi-crystalline structure [39]. A sharp peak at 2θ of about 20.12° means the β-sheet structure of the WPI [40]. For GEN (Fig. 4 (B, b)), diffraction peaks were seen at 2θ of 38.38°, 44.6°, 64.88°, and 77.92°. The XRD curve of PVA (Fig. 4 (B, c)), at 2θ = 19.88° and 22.88°, indicates strong crystalline reflections. These peaks represent reflections from a monoclinic unit cell (1 0 1) and (2 0 0) and are characteristic of PVA [41]. The peak at 38.02° is related to the semi-crystalline structure of PVA polymer. The semi-crystalline structure that forms the characteristic of PVA is maintained by intramolecular and intermolecular hydrogen bonds [42]. Another diffraction peak for PVA is observed at 2θ = 44.28° [35]. In the XRD spectrum of HA shown in Fig. 4 (B, d), all of the crystallographic planes (0 0 2), (2 1 1), (1 1 2), and (3 0 0) corresponding at 2θ = 25.96°, 31.84°, 32.26°, and 32.98° diffraction peaks, respectively [43]. The obtained results from the XRD spectrum indicate that HA's diffraction peaks seen at 2θ = 25.96°, 31.84°, 32.26°, and 32.98° were seen at the same peak points in Fig. 4 (B, e), (B, f) and (B, g). This is because the HA has the highest ratio in the production of composites and originates from the same amount of HA used in PVA/WPI/HA, PVA/WPI/HA/6GEN, and PVA/WPI/HA/12GEN composites. The diffraction peaks of the GEN at 2θ = 64.88° and 77.92° are seen in the same peak points in Fig. 4 (B, f), (B, g), while the peaks cannot be seen in Fig. 4 (B, e). The diffraction peaks at these points indicate the presence of gentamicin drugs which are loaded to the PVA/WPI/HA/6GEN and PVA/WPI/HA/12GEN composites.

3.5. Differential scanning calorimetry (DSC)

DSC thermograms were shown for PVA/WPI/HA, PVA/WPI/HA/6GEN and PVA/WPI/HA/12GEN in Fig. 4 (C). Highly crystalline PVA has a melting point of approximately 200 °C [44]. The melting point for the PVA/WPI/HA and PVA/WPI/HA/6GEN composites shown in Fig. 4 (C, a) and (C, b) was also very close to 200 °C, which means the produced composites were highly crystalline. Fig. 4 (C, a) is more visible than the peak in Fig. 4 (C, b). With the addition of gentamicin drugs to the produced scaffolds, the highly crystalline structure of PVA became less noticeable, and the crystal structure decreased. In hydroxyapatite

powder, it is known that there are two types of water prepared by the precipitation method, absorbed water and crystallisation water [45]. The peak seen at 58.1 °C is associated with the elimination of surface absorbed water from the hydroxyapatite [46]. When the temperature is increased from 200 °C to 400 °C, the peak observed at 249 °C indicates the loss of the crystallisation water [45]. It is seen that the degradation steps of the produced scaffolds are in the range of 280–380 °C degrees [47]. The melting point of the composite in Fig. 4 (C, c) is between 240 and 260 °C. The reason for this is the melting peak of the gentamicin drug. Since the composite in Fig. 4 (C, c) contains more drugs than the composite in Fig. 4 (C, b), the effect of the drug amount is seen on the melting peak of composites.

3.6. Mechanical properties of the scaffolds

Compression test results performed to determine the mechanical properties of scaffolds are given in Table 3. Table 3 show that PVA/WPI/HA has the highest compressive strength (1.28 MPa). PVA/WPI/HA/6GEN and PVA/WPI/HA/12GEN have equally lower compressive strengths (1.22 MPa). This shows that the compressive strength values decrease with the addition of gentamicin drugs to the tissue scaffolds. According to other studies on bone tissue, it is known that drug loading on structures causes adverse effects on the compressive strength [48]. However, when the strain values (%) of the constructs were compared, it was seen that the PVA/WPI/HA structure had the highest strain (12.89%). The lowest strain (8.70 %) was seen in the PVA/WPI/HA/12GEN structure. It can be indicated that loading gentamicin drug to PVA/WPI/HA scaffolds induced a drop in the strain values of the structures. The decrease in the strain values affects the brittleness of the substance [49]. When all these compressive strengths and strain values are evaluated together, it has been shown that the PVA/WPI/HA scaffold has the best mechanical properties thanks to its ability to deform to a great extent and absorb the force before breaking. Gerhardt et al. reported in their study that the compressive strength of trabecular bone, which is one of the bone tissue types, is in the range of 0.1–16 MPa [50]. As a result of the compression test in this study, compressive strength values of the produced scaffolds showed that they are suitable for bone tissue applications in terms of mechanical properties.

3.7. Swelling and degradation behaviour of scaffolds

The ability of tissue engineering scaffolds to absorb water helps provide nutrients and oxygen to the interior [51]. It is also an essential property for drug-loaded scaffolds as swelling rates significantly influence the controlled drug delivery behaviour [52]. Fig. 5 (a) represents the water uptake ratios of the 3D-printed scaffolds at 37 ∘C. In the PVA/WPI/HA scaffold, the swelling rate at the end of the 1st day increases to approximately 180%. It can be said that the swelling rates of drug-loaded PVA/WPI/HA/6GEN and PVA/WPI/HA/12GEN scaffolds at the end of the 1st day are very close to pure scaffolds but slightly higher. According to these results, it can be said that gentamicin loading does not seriously affect the water absorption property of the scaffold. It was observed that all three scaffolds showed swelling behaviour until the end of the 3rd day and the swelling rates decreased after the third day. The increase in the swelling rate in the first days is attributed to the migration of water into the polymeric network driven by the osmotic pressure. The next decrease in the swelling rate after the 3rd day is due to the onset of a partial degradation [53].

Scaffolds produced for tissue engineering are expected to have a certain degradation property to allow the cell and provide sufficient space for growth and tissue formation [54]. The deterioration of structures exposed to PBS and weight loss over time are essential criteria for the tissue engineering [21]. According to Fig. 5 (b), the degradation analysis continued for 10 days, showing that all three PVA/WPI/HA, PVA/WPI/HA/6GEN, and PVA/WPI/HA/12GEN scaffolds exhibit similar degradation behaviour. At the end of the 10th day, the degradation rate of all three scaffolds reached approximately 55%. Just as with swelling, although there is a small difference in the degradation rate of drug-loaded scaffolds compared to pure scaffolds, it can be argued that drug loading almost does not change the degradation behaviour. In all three scaffolds, it can be observed that the swelling feature and the degradation feature are proportional from day today. The results obtained are supported by the statement in the literature that materials that absorb more water show good swelling properties and generally deteriorate faster [55].

Table 3
Compressive testing results for PVA/WPI/HA, PVA/WPI/HA/6GEN and PVA/WPI/HA/12GEN.

Scaffolds	Compressive Strength (MPa)	Strain (%)
PVA/WPI/HA	1.28 ± 0.029	12.89 ± 1.020
PVA/WPI/HA/6GEN	1.22 ± 0.009	10.57 ± 3.830
PVA/WPI/HA/12GEN	1.22 ± 0.039	8.70 ± 1.028

3.8. Encapsulation efficiency and drug release behaviours of scaffolds

In this study, in vitro, drug release tests were performed to investigate the release properties of gentamicin from 3D-printed scaffolds. The gentamicin release profile from the PVA/WPI/HA/6GEN and PVA/WPI/HA/12GEN scaffolds was also examined in a 37 °C shaker. To mimic physiological conditions, releases were investigated in PBS at pH 7.4, and the results are shown in Fig. 6. A calibration curve for gentamicin was created by preparing three different ratios (0.25, 0.5, and 1 μg/ml) from the initially prepared stock solution (Fig. 6 (a)). According to the peak value obtained at 196 nm for gentamicin, the absorbance graph ($R^2 = 0.9969$) is drawn in Fig. 6 (b). The encapsulation efficiency (EE) of gentamicin into the PVA/WPI/HA/6GEN and PVA/WPI/HA/12GEN scaffolds was determined. Encapsulation efficiency of the 3D-printed scaffolds was determined as 52.74% and 35.36%, respectively Fig. 6 (c). The decrease in encapsulation efficiency due to several different factors can be attributed to the maximum loading of the drug and the saturation point. For this reason, it can be said that the percent encapsulation efficiency is lower when a high amount of drug is added [56]. According to the cumulative release, the graph obtained, it is observed that a burst release occurs in the PVA/WPI/HA/6GEN scaffold until the 12th hour, and 63.80% of the drug is released Fig. 6 (d). A similar situation exists in the PVA/WPI/HA/12GEN scaffold. It is observed that 57.54% of the drug is released in the first 12 h. However, when the total cumulative release graph is examined, the completion of drug release from the PVA/WPI/HA/6GEN and PVA/WPI/HA/12GEN scaffolds to 100% continues until the 240th and 264th hours, respectively. As a result, it can be said that a controlled release lasting up to 10 days was achieved in the scaffolds obtained. According to the results obtained, gentamicin, which is water-soluble and hydrophilic, exhibited a rapid release profile from both scaffolds in the first 12 h. In 3D-printed scaffolds, although an immediate release occurred in the first hours in PBS, it is seen that the release is more controlled and lasts longer because cross-linking happens by exposure to glutaraldehyde vapour. It is known that after the cross-linking application, the structures become denser, and the release of the drug is more difficult than in an uncross-linked network [57]. Cui et al. study stated that cross-linking causes lower drug diffusion and prolongs the release [58]. Drug release kinetics of 3D-printed scaffolds loaded with GEN at different rates. It was analysed according to Zero-Order, First-Order, Korsmeyer-Peppas, Higuchi, and Hixon-Crowell models (Fig. 7). The kinetic constants and regression coefficients (R^2) obtained from the graphs for the scaffolds are shown in Table 4. The highest correlation coefficient obtained was determined as a mathematical model showing drug release kinetics from scaffolds. The highest correlation coefficients in PVA/WPI/HA/6GEN and PVA/WPI/HA/12GEN scaffolds were obtained as $R^2 = 0.9926$ and $R^2 = 0.9855$, respectively. Accordingly, GEN release from both scaffolds can be

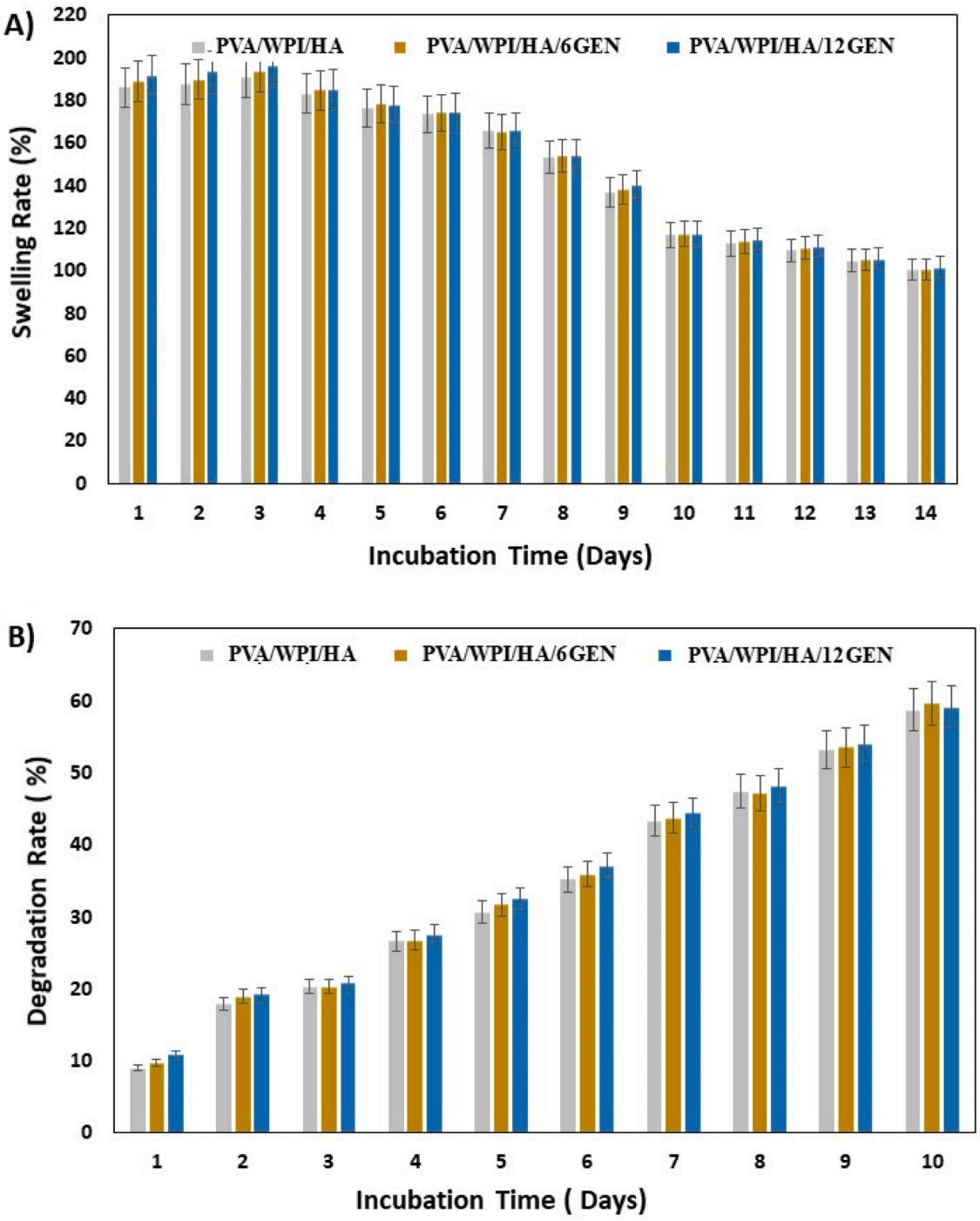

Fig. 5. Swelling(a) and Degradation(b) graphics of PVA/WPI/HA, PVA/WPI/HA/6GEN, and PVA/WPI/HA/12GEN scaffolds.

explained by the Korsmeyer-Peppas kinetic model. The ranges of "n" values associated with the Korsmeyer-Peppas model and corresponding to different transport mechanisms are shown in Table 5 [21]. According to the "n" value, which illuminates the drug release mechanism from the polymeric material, it can be said that the release from both scaffolds occurs according to the Super case II transport mechanism.

3.9. MTT analysis and cell attachment studies

The viability of the osteoblast cells on 3D-printed PVA/WPI/HA, PVA/WPI/HA/6GEN, and PVA/WPI/HA/12GEN scaffolds for bone tissue engineering were determined with MTT analysis. MTT assay was carried out for 1, 4, and 7 days incubation to determine the osteoblast cell viability of scaffolds. Cell viability of the produced 3D-printed scaffolds was calculated relative to the PVA/WPI/HA scaffold. The cell viability of 3D-printed scaffolds was similar, and the cellular viability of all materials was higher than control scaffolds for a 3-day treatment. Although the cell viability of the PVA/WPI/HA/6GEN scaffold increased slightly on the 7th day, it was observed that the cell viability of the PVA/WPI/HA/12GEN scaffold decreased slightly on the 7th-day treatment. According to the results shown in Fig. 8 (A), it is seen that all of the PVA/WPI/HA, PVA/WPI/HA/6GEN, and PVA/WPI/HA/12GEN scaffolds developed did not cause any toxicity on osteoblast cells. Kumar et al. demonstrated that osteoblastic growth was supported in both charged

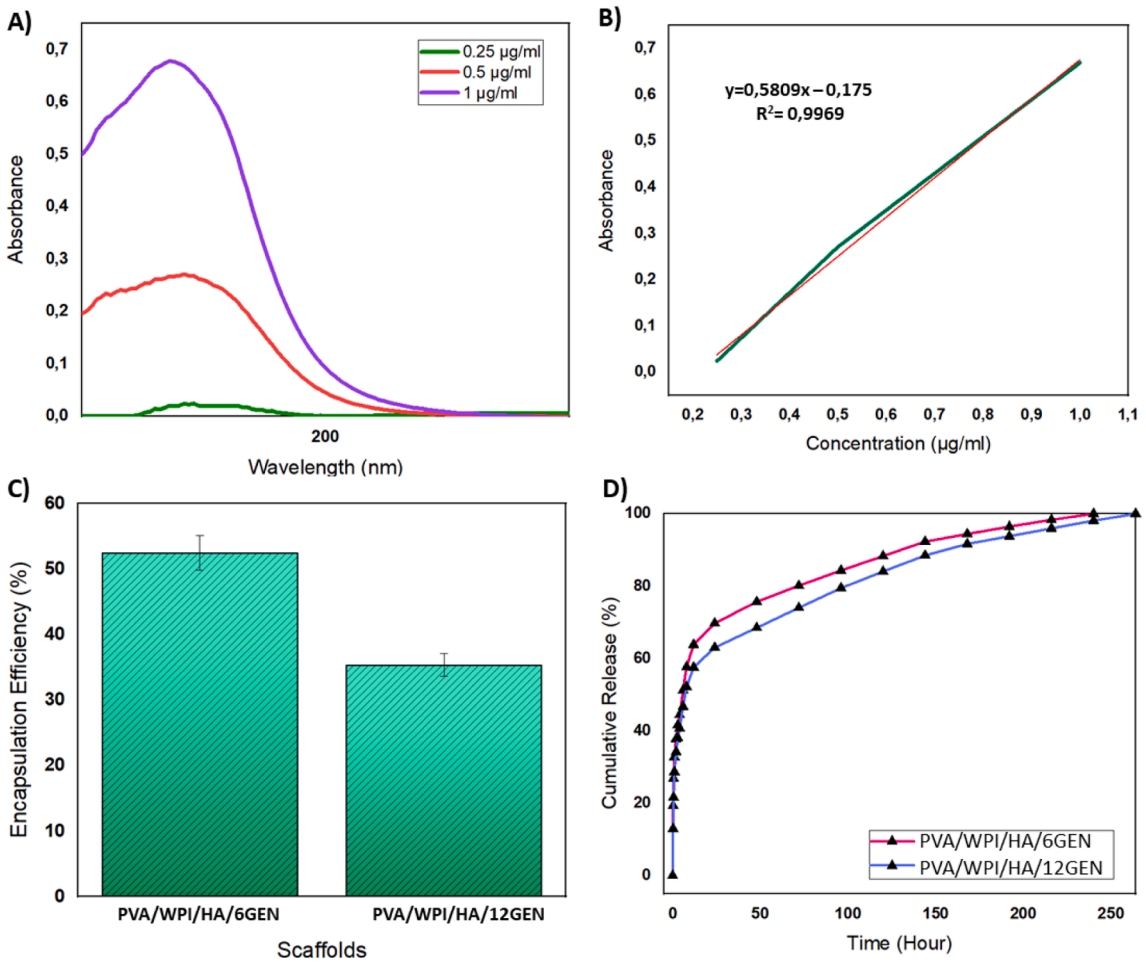

Fig. 6. In vitro drug release profiles of scaffolds: Absorption spectra of gentamicin at different concentrations (a), gentamicin calibration curve (b), encapsulation efficiency of gentamicin-loaded scaffolds (c), drug release profiles from the scaffolds that have the concentration of gentamicin (d). All the measurements were repeated three times, and the errors were less than 5%.

and uncharged HA samples and caused an increase in cell proliferation for 7 days. In addition, it can be said that both negative and positive charges on the HA surface cause an increase in the metabolic activity of the osteoblast cell [59]. In addition, studies showing that whey protein increases osteoblast cell proliferation and differentiation and is a promoter of osteoblast growth support the non-toxicity of MTT results [60].

Furthermore, osteoblast cell interactions with 3D-printed scaffolds were examined by SEM imaging. As shown in Fig. 8 (B), osteoblast cells successfully adhered to scaffolds after 1, 3, and 7 days of incubation. In addition, 7-day incubation images prove that osteoblasts from filopodia extensions, which is considered a sign of biocompatibility, show a healthy attachment behaviour to the surface they are located on and not under stress. Osteoblast cell filopodia extensions are observed on all scaffolds. This suggests that HA could provide a suitable microenvironment for cell development. Hydroxyapatite is widely recognised as an osteoconductive biomaterial associated with rapid bone healing and close adaptation of bone tissue [61]. Gutiérrez-Prieto et al. planted cells on prepared scaffolds to investigate osteoblast cell morphology, adherence, and viability. The results also support this study, and HA was the material that showed the best cell adhesion among the different polymers [62].

4. Conclusions

In this study, PVA/WPI/HA, PVA/WPI/HA/6GEN and PVA/WPI/HA/12GEN composite scaffolds for bone tissue engineering were successfully produced with 3D printing technology. In order to prevent the rapid deterioration of the produced composite scaffolds and to increase their mechanical strength, crosslinking was done with GA vapour. Addition of GEN to the solution consisting of PVA, WPI, and HA caused an increase in viscosity. When the SEM images of the obtained composite scaffolds were examined, it was seen that they had the desired porosity and properties for bone tissue engineering applications. In addition, the diameters of the PVA/WPI/HA, PVA/WPI/HA/6GEN and PVA/WPI/HA/12GEN scaffolds were 716.25 ± 101.17 µm, 678.61 ± 66.37 µm and 675.55 ± 60.71 µm, respectively. The PVA/WPI/HA/12GEN composite scaffold was excellently obtained with its 675 µm pore size which means that according to the literature, it has a suitable pore size to provide cellular growth and bone ingrowth for bone tissue engineering. XRD and FTIR results showed a strong interaction between PVA, WPI, HA and GEN. According to the DSC analysis, the addition of GEN to the composite scaffolds disrupted the highly crystalline structure of PVA. However, swelling and degradation did not affect the behavior much. At the end of the 10th day, it can be said that approximately 55% of the scaffolds have deteriorated. The addition of GEN at different concentrations adversely affected the compressive strength and strain values of composite scaffolds, but still suitable for mechanical properties for human trabecular bone (0.1–16 MPa). When drug release results were analyzed, the scaffolds showed a controlled release profile extending up to 240 and 264 h. Considering the highest correlation number, both scaffolds exhibit the Korsmeyer-Peppas mathematical kinetic model. The obtained cell test results proved that biocompatible scaffolds were produced, and after 7 days of incubation, osteoblast cells formed filopodia extensions and exhibited healthy cell attachment.

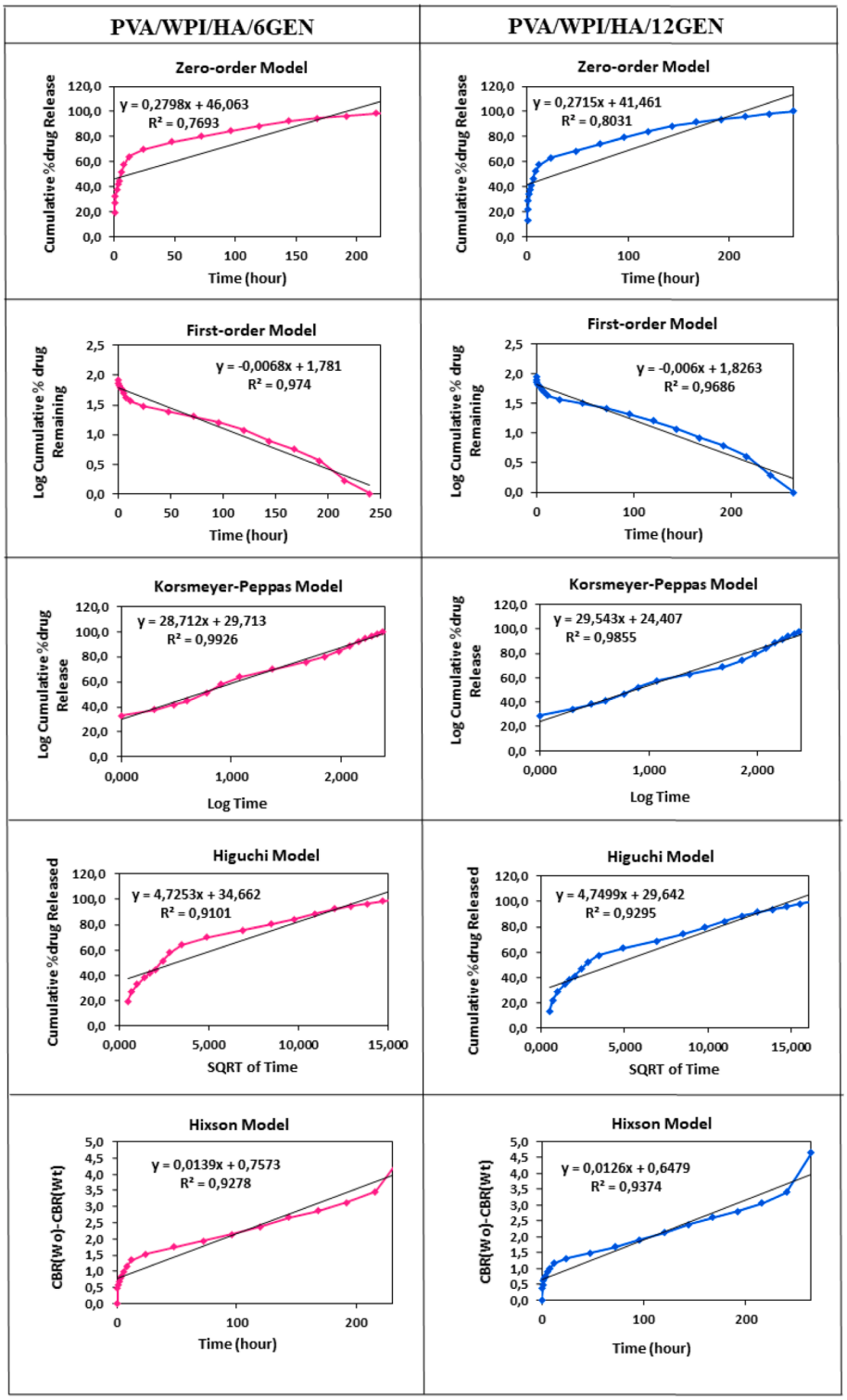

Fig. 7. The kinetic release models of GEN release profiles from the PVA/WPI/HA/6GEN and PVA/WPI/HA/12GEN scaffolds; Zero-order, First-order, Korsmeyer-Peppas, Higuchi, and Hixson-Crowell models.

Table 4
Results of mathematical drug release models for all scaffolds: PVA/WPI/HA/6GEN, PVA/WPI/HA/12GEN.

Sample	Korsmeyer-Peppas		Zero-Order		First-Order		Higuchi		Hixson-Crowell	
	R^2	n	R^2	K_0	R^2	K_1	R^2	K_h	R^2	K_{hc}
PVA/WPI/HA/6GEN	0,9926	28,712	0,7693	0,2798	0,974	−0,0068	0,9101	4,7253	0,9278	0,0139
PVA/WPI/HA/12GEN	0,9855	29,543	0,8031	0,2715	0,9686	−0,006	0,9295	4,7499	0,9374	0,0126

Table 5
Transport mechanisms types according to the ranges of n value.

The ranges of n values	Transport mechanisms
$0.45 \leq n$	Fickian diffusion mechanism
$0.45 < n < 0.89$	Non-Fickian transport
$n = 0.89$	Case II (relaxational) transport
$n > 0.89$	Super case II transport

Considering all the results, GEN-loaded 3D PVA/WPI/HA composite scaffolds may be a promising innovation for bone defect repair in bone tissue engineering applications.

CRediT authorship contribution statement

Tufan Arslan Tut: Methodology, Investigation. **Sumeyye Cesur:** Investigation. **Elif Ilhan:** Investigation, Methodology. **Ali Sahin:** Methodology. **Onur Samet Yildirim:** Investigation, Methodology.

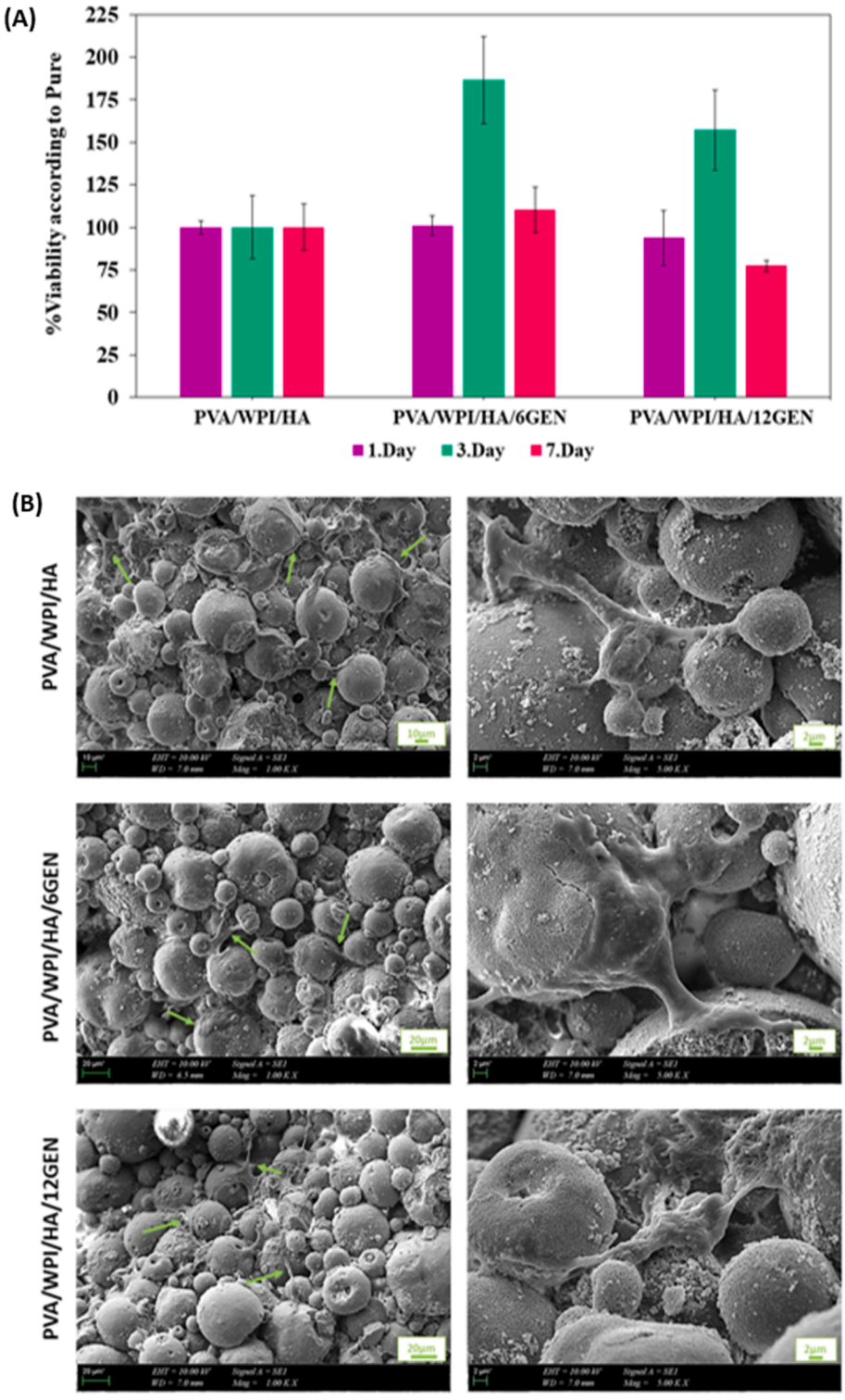

Fig. 8. (A) Cell viability results of 1-day, 3-day, and 7-day treated scaffolds. PVA/WPI/HA scaffold was accepted as a control, and the calculations were compared with the controlled material. Results are the average value of three different technical replicates, which is estimated by relative cell viability ratio compared to Day 1 PVA/WPI/HA treatment PVA/WPI/HA, PVA/WPI/HA/6GEN, PVA/WPI/HA/12GEN composite scaffolds. (B) SEM images of osteoblast cells on PVA/WPI/HA PVA/WPI/HA, PVA/WPI/HA/6GEN, and PVA/WPI/HA/12GEN scaffolds.

Oguzhan Gunduz: Conceptualization, Methodology.

Declaration of Competing Interest

The authors declare that they have no known competing financial interests or personal relationships that could have appeared to influence the work reported in this paper.

Acknowledgements

This study was funded by TUBITAK, 2209-A - Research Project Support Program for Undergraduate Students, grant no: 1919B012111324.

References

[1] W. Xu, X. Liao, B. Li, T. Li, Biomaterials and bone tissue engineering, in: Proc. 2011 Int. Symp. Bioelectron. Bioinformatics, ISBB 2011, 2011. doi:10.1109/ISBB.2011.6107687.
[2] S. Cesur, F.N. Oktar, N. Ekren, O. Kilic, D.B. Alkaya, S.A. Seyhan, Z.R. Ege, C.-C. Lin, S.E. Kuruca, G. Erdemir, O. Gunduz, Preparation and characterization of electrospun polylactic acid/sodium alginate/orange oyster shell composite nanofiber for biomedical application, J. Aust. Ceram. Soc. (2019), https://doi.org/10.1007/s41779-019-00363-1.
[3] G.L. Koons, M. Diba, A.G. Mikos, Materials design for bone-tissue engineering, Nat. Rev. Mater. (2020), https://doi.org/10.1038/s41578-020-0204-2.
[4] N. Shahrubudin, T.C. Lee, R. Ramlan, An overview on 3D printing technology: technological, materials, and applications, Proc. Manuf. 35 (2019) 1286–1296, https://doi.org/10.1016/j.promfg.2019.06.089.
[5] J. Gopinathan, I. Noh, Recent trends in bioinks for 3D printing, Biomater. Res. (2018), https://doi.org/10.1186/s40824-018-0122-1.
[6] Z. Xu, N. Wang, Y. Ma, H. Dai, B. Han, Preparation and study of 3D printed dipyridamole/β-tricalcium phosphate/ polyvinyl alcohol composite scaffolds in bone tissue engineering, J. Drug Deliv. Sci. Technol. (2022), https://doi.org/10.1016/j.jddst.2021.103053.
[7] S. Alinavaz, G.R. Mahdavinia, H. Jafari, M. Hazrati, A. Akbari, Hydroxyapatite (HA)-based hybrid bionanocomposite hydrogels: Ciprofloxacin delivery, release kinetics and antibacterial activity, J. Mol. Struct. (2021), https://doi.org/10.1016/j.molstruc.2020.129095.
[8] H. Kobayashi, M. Kato, T. Taguchi, T. Ikoma, H. Miyashita, S. Shimmura, K. Tsubota, J. Tanaka, Collagen immobilized PVA hydrogel-hydroxyapatite composites prepared by kneading methods as a material for peripheral cuff of artificial cornea, Mater. Sci. Eng. C 24 (6–8) (2004) 729–735, https://doi.org/10.1016/j.msec.2004.08.038.
[9] M.A. Nazeer, O.C. Onder, I. Sevgili, E. Yilgor, I.H. Kavakli, I. Yilgor, 3D printed poly(lactic acid) scaffolds modified with chitosan and hydroxyapatite for bone repair applications, Mater. Today Commun. (2020), https://doi.org/10.1016/j.mtcomm.2020.101515.
[10] Q. Wei, Y. Wang, W. Chai, Y. Zhang, X. Chen, Molecular dynamics simulation and experimental study of the bonding properties of polymer binders in 3D powder printed hydroxyapatite bioceramic bone scaffolds, Ceram. Int. (2017), https://doi.org/10.1016/j.ceramint.2017.07.082.
[11] M.A. Nazeer, E. Yilgor, M.B. Yagci, U. Unal, I. Yilgor, Effect of reaction solvent on hydroxyapatite synthesis in sol–gel process, R. Soc. Open Sci. (2017), https://doi.org/10.1098/rsos.171098.
[12] S.A. Seyhan, D.B. Alkaya, S. Cesur, F.N. Oktar, O. Gunduz, Preparation and characterization of pure natural hydroxyapatite derived from seashells for controlled drug delivery, J. Aust. Ceram. Soc. 58 (4) (2022) 1231–1240, https://doi.org/10.1007/s41779-022-00739-w.
[13] S.T. Bendtsen, S.P. Quinnell, M. Wei, Development of a novel alginate-polyvinyl alcohol-hydroxyapatite hydrogel for 3D bioprinting bone tissue engineered scaffolds, J. Biomed. Mater. Res. - Part A. (2017), https://doi.org/10.1002/jbm.a.36036.
[14] S. Mistry, R. Roy, B. Kundu, S. Datta, M. Kumar, A. Chanda, D. Kundu, Clinical outcome of hydroxyapatite coated, bioactive glass coated, and machined Ti6Al4V threaded dental implant in human jaws: a short-term comparative study, Implant Dent. (2016), https://doi.org/10.1097/ID.0000000000000376.
[15] Whey protein, Altern. Med. Rev. (2008). 10.1533/9780857093639.30.
[16] R. Llamas-Unzueta, M. Suárez, A. Fernández, R. Díaz, M.A. Montes-Morán, J. Angel Menéndez, Whey-derived porous carbon scaffolds for bone tissue engineering, Biomedicines. (2021), https://doi.org/10.3390/biomedicines9091091.
[17] M. Betz, C.A. García-González, R.P. Subrahmanyam, I. Smirnova, U. Kulozik, Preparation of novel whey protein-based aerogels as drug carriers for life science applications, J. Supercrit. Fluids. (2012), https://doi.org/10.1016/j.supflu.2012.08.019.
[18] T.E.L. Douglas, M. Vandrovcová, N. Kročilová, J.K. Keppler, J. Zárubová, A. G. Skirtach, L. Bačáková, Application of whey protein isolate in bone regeneration: effects on growth and osteogenic differentiation of bone-forming cells, J. Dairy Sci. (2018), https://doi.org/10.3168/jds.2017-13119.
[19] M. Dziadek, R. Kudlackova, A. Zima, A. Slosarczyk, M. Ziabka, P. Jelen, S. Shkarina, A. Cecilia, M. Zuber, T. Baumbach, M.A. Surmeneva, R.A. Surmenev, L. Bacakova, K. Cholewa-Kowalska, T.E.L. Douglas, Novel multicomponent organic–inorganic WPI/gelatin/CaP hydrogel composites for bone tissue engineering, J. Biomed. Mater. Res. - Part A. (2019), https://doi.org/10.1002/jbm.a.36754.
[20] P. Rajasekaran, D. Crich, Synthesis of gentamicin minor components: gentamicin B1 and gentamicin X2, Org. Lett. (2020), https://doi.org/10.1021/acs.orglett.0c01107.
[21] E. Saylam, Y. Akkaya, E. Ilhan, S. Cesur, E. Guler, A. Sahin, E. Cam, N. Ekren, F. Nuzhet Oktar, O. Gunduz, D. Ficai, A. Ficai, P. Calandra, D. Lombardo, Levodopa-Loaded 3D-Printed Poly (Lactic) Acid/Chitosan Neural Tissue Scaffold as a Promising Drug Delivery System for the Treatment of Parkinsons Disease, Appl. Sci. 2021, Vol. 11, Page 10727. 11 (2021) 10727. doi:10.3390/APP112210727.
[22] S. Cesur, M.E. Cam, F.S. Sayın, S. Su, A. Harker, M. Edirisinghe, O. Gunduz, Metformin-loaded polymer-based microbubbles/nanoparticles generated for the treatment of type 2 diabetes mellitus, Langmuir. (2021), https://doi.org/10.1021/acs.langmuir.1c00587.
[23] K. Aranci, M. Uzun, S. Su, S. Cesur, S. Ulag, A. Amin, M.M. Guncu, B. Aksu, S. Kolayli, C.B. Ustundag, J.C. Silva, D. Ficai, A. Ficai, O. Gunduz, 3D propolis-sodium alginate scaffolds: influence on structural parameters, release mechanisms, cell cytotoxicity and antibacterial activity, Molecules. (2020), https://doi.org/10.3390/molecules25215082.
[24] C. Kalkandelen, S. Ulag, B. Ozbek, G.O. Eroglu, D. Ozerkan, S.E. Kuruca, F. N. Oktar, M. Sengor, O. Gunduz, 3D printing of gelatine/alginate/β-tricalcium phosphate composite constructs for bone tissue engineering, ChemistrySelect. (2019), https://doi.org/10.1002/slct.201902878.
[25] E. Saylam, Y. Akkaya, E. Ilhan, S. Cesur, E. Guler, A. Sahin, M.E. Cam, N. Ekren, F. N. Oktar, O. Gunduz, D. Ficai, A. Ficai, Levodopa-loaded 3d-printed poly (Lactic) acid/chitosan neural tissue scaffold as a promising drug delivery system for the treatment of Parkinson's disease, Appl. Sci. (2021), https://doi.org/10.3390/app112210727.
[26] E. Ilhan, S. Cesur, E. Guler, F. Topal, D. Albayrak, M.M. Guncu, M.E. Cam, T. Taskin, H.T. Sasmazel, B. Aksu, F.N. Oktar, O. Gunduz, Development of Satureja cuneifolia-loaded sodium alginate/polyethylene glycol scaffolds produced by 3D-printing technology as a diabetic wound dressing material, Int. J. Biol. Macromol. (2020), https://doi.org/10.1016/j.ijbiomac.2020.06.086.
[27] J. Chen, E.S. Garcia, S.C. Zimmerman, Intramolecularly cross-linked polymers: from structure to function with applications as artificial antibodies and artificial enzymes, Acc. Chem. Res. (2020), https://doi.org/10.1021/acs.accounts.0c00178.
[28] A. Morawska-Chochól, Assessment of the microstructure and mechanical properties of porous gelatin scaffolds, Eng. Biomater. 160 (2021) 22–27. doi:10.34821/eng.biomat.160.2021.22-27.
[29] H. Sun, C. Hu, C. Zhou, L. Wu, J. Sun, X. Zhou, F. Xing, C. Long, Q. Kong, J. Liang, Y. Fan, X. Zhang, 3D printing of calcium phosphate scaffolds with controlled release of antibacterial functions for jaw bone repair, Mater. Des. (2020), https://doi.org/10.1016/j.matdes.2020.108540.
[30] I. Sopyan, Gunawan, Development of porous calcium phosphate bioceramics for bone implant applications: a review, recent patents, Mater. Sci. (2013), https://doi.org/10.2174/1874464811306990012.
[31] G. Gbassi, F. Yolou, S. Sarr, P. Atheba, C. Amin, M. Ake, Whey proteins analysis in aqueous medium and in artificial gastric and intestinal fluids, Int. J. Biol. Chem. Sci. (2012), https://doi.org/10.4314/ijbcs.v6i4.38.
[32] R. Batul, M. Bhave, P.J. Mahon, A. Yu, Polydopamine nanosphere with in-situ loaded gentamicin and its antimicrobial activity, Molecules. (2020), https://doi.org/10.3390/molecules25092090.
[33] A. Rapacz-Kmita, E. Stodolak-Zych, M. Ziabka, A. Rozycka, M. Dudek, Instrumental characterization of the smectite clay-gentamicin hybrids, Bull. Mater. Sci. (2015), https://doi.org/10.1007/s12034-015-0943-7.
[34] A. Kharazmi, N. Faraji, R.M. Hussin, E. Saion, W.M.M. Yunus, K. Behzad, Structural, optical, opto-thermal and thermal properties of ZnS-PVA nanofluids synthesized through a radiolytic approach, Beilstein J. Nanotechnol. (2015), https://doi.org/10.3762/bjnano.6.55.
[35] S. Cesur, M.E. Cam, F.S. Sayin, O. Gunduz, Electrically controlled drug release of donepezil and BiFeO3 magnetic nanoparticle-loaded PVA microbubbles/nanoparticles for the treatment of Alzheimer's disease, J. Drug Deliv. Sci. Technol. (2022), https://doi.org/10.1016/j.jddst.2021.102977.
[36] A.M. Cakmak, S. Unal, A. Sahin, F.N. Oktar, M. Sengor, N. Ekren, O. Gunduz, D. M. Kalaskar, 3d printed polycaprolactone/gelatin/bacterial cellulose/hydroxyapatite composite scaffold for bone tissue engineering, Polymers (Basel). (2020), https://doi.org/10.3390/polym12091962.
[37] H. Gheisari, E. Karamian, M. Abdellahi, A novel hydroxyapatite -Hardystonite nanocomposite ceramic, Ceram. Int. (2015), https://doi.org/10.1016/j.ceramint.2015.01.033.
[38] Z. Ghasempour, S. Khodaeivandi, H. Ahangari, H. Hamishehkar, S. Amjadi, E. Moghaddas Kia, A. Ehsani, Characterization and optimization of persian gum/whey protein bionanocomposite films containing betanin nanoliposomes for food packaging utilization, J. Polym. Environ. (2022), https://doi.org/10.1007/s10924-021-02367-0.
[39] N. Karimi, A. Alizadeh, H. Almasi, S. Hanifian, Preparation and characterization of whey protein isolate/polydextrose-based nanocomposite film incorporated with cellulose nanofiber and L. plantarum: a new probiotic active packaging system, LWT. (2020), https://doi.org/10.1016/j.lwt.2019.108978.
[40] Z. Hazrati, A. Madadlou, Gelation by bioactives: characteristics of the cold-set whey protein gels made using gallic acid, Int. Dairy J. (2021), https://doi.org/10.1016/j.idairyj.2020.104952.

[41] C.M. Tang, Y.H. Tian, S.H. Hsu, Poly(vinyl alcohol) nanocomposites reinforced with bamboo charcoal nanoparticles: mineralization behavior and characterization, Materials (Basel). (2015), https://doi.org/10.3390/ma8084895.
[42] S.B. Aziz, R.T. Abdulwahid, M.A. Rasheed, O.G.H. Abdullah, H.M. Ahmed, Polymer blending as a novel approach for tuning the SPR peaks of silver nanoparticles, Polymers (Basel). (2017), https://doi.org/10.3390/polym9100486.
[43] V. Mišković-Stanković, S. Eraković, A. Janković, M. Vukašinović-Sekulić, M. Mitrić, Y.C. Jung, S.J. Park, K.Y. Rhee, Electrochemical synthesis of nanosized hydroxyapatite/ graphene composite powder, Carbon Lett. (2015), https://doi.org/10.5714/CL.2015.16.4.233.
[44] J. Namkaew, P. Laowpanitchakorn, N. Sawaddee, S. Jirajessada, S. Honsawek, S. Yodmuang, Carboxymethyl cellulose entrapped in a poly(Vinyl) alcohol network: plant-based scaffolds for cartilage tissue engineering, Molecules. (2021), https://doi.org/10.3390/molecules26030578.
[45] R. Quan, C. Wang, H. Wang, X. Wei, Z. Zhao, Investigation on high-temperature decomposition and regeneration characteristics of hydroxyapatite powders and sinters, Asian J. Chem. (2013). doi:10.14233/ajchem.2013.15148.
[46] M. Prakasam, M. Popescu, R. Piticescu, A. Largeteau, Fabrication methodologies of biomimetic and bioactive scaffolds for tissue engineering applications, Scaffolds Tissue Eng. - Mater. Technol. Clin. Appl. (2017), https://doi.org/10.5772/intechopen.70707.
[47] F.C. Kenechukwu, M.A. Momoh, P.O. Nnamani, A.A. Attama, Solid lipid microdispersions (SLMs) based on PEGylated solidified reverse micellar solutions (SRMS): a novel carrier system for gentamicin, Drug Deliv. (2015), https://doi.org/10.3109/10717544.2014.900152.
[48] Y. Chang, C.-L. Tai, P.-H. Hsieh, S.W.N. Ueng, Gentamicin in bone cement, Bone Joint Res. (2013), https://doi.org/10.1302/2046-3758.210.2000188.
[49] D.A. Brown, E.W. Lee, C.T. Loh, S.T. Kee, A new wave in treatment of vascular occlusive disease: biodegradable stents-clinical experience and scientific principles, J. Vasc. Interv. Radiol. (2009), https://doi.org/10.1016/j.jvir.2008.11.007.
[50] L.C. Gerhardt, A.R. Boccaccini, Bioactive glass and glass-ceramic scaffolds for bone tissue engineering, Materials (Basel). (2010), https://doi.org/10.3390/ma3073867.
[51] E. Ilhan, S. Ulag, A. Sahin, B.K. Yilmaz, N. Ekren, O. Kilic, M. Sengor, D. M. Kalaskar, F.N. Oktar, O. Gunduz, Fabrication of tissue-engineered tympanic membrane patches using 3D-Printing technology, J. Mech. Behav. Biomed. Mater. 114 (2020) 104219, https://doi.org/10.1016/j.jmbbm.2020.104219.
[52] J. Zhang, Q. Wang, A. Wang, In situ generation of sodium alginate/hydroxyapatite nanocomposite beads as drug-controlled release matrices, Acta Biomater. 6 (2) (2010) 445–454, https://doi.org/10.1016/j.actbio.2009.07.001.
[53] W.-F. Lee, R.-J. Wu, Superabsorbent polymeric materials. II. Swelling behavior of crosslinked poly[sodium acrylate-co-3-dimethyl(methacryloyloxyethyl) ammonium propane sulfonate] in aqueous salt solution, J. Appl. Polym. Sci. 64 (9) (1997) 1701–1712.
[54] S. Cesur, S. Ulag, L. Ozak, A. Gumussoy, S. Arslan, B.K. Yilmaz, N. Ekren, M. Agirbasli, D.M. kalaskar, O. Gunduz, Production and characterization of elastomeric cardiac tissue-like patches for Myocardial Tissue Engineering, Polym. Test. 90 (2020) 106613. doi:10.1016/j.polymertesting.2020.106613.
[55] D. Wang, D.J.T. Hill, H. Peng, A. Symons, S. Varanasi, A.K. Whittaker, F. Rasoul, Development of injectable biodegradable multi-arms PEG-based hydrogels: swelling and degradation investigations, Macromol. Symp. (2010), https://doi.org/10.1002/masy.201051033.
[56] C.G. Keum, Y.W. Noh, J.S. Baek, J.H. Lim, C.J. Hwang, Y.G. Na, S.C. Shin, C. W. Cho, Practical preparation procedures for docetaxel-loaded nanoparticles using polylactic acid-co-glycolic acid, Int. J. Nanomed. (2011), https://doi.org/10.2147/ijn.s24547.
[57] A. Kumar, M. Pandey, K. Mamman, S. Saraf, Synthesis of fast swelling superporous hydrogel: effect of concentration of crosslinker and acdisol on swelling ratio and mechanical strength, Int. J. Drug Deliv. 2 (2011), https://doi.org/10.5138/ijdd.2010.0975.0215.02022.
[58] Z. Cui, Z. Zheng, L. Lin, J. Si, Q. Wang, X. Peng, W. Chen, Electrospinning and crosslinking of polyvinyl alcohol/chitosan composite nanofiber for transdermal drug delivery, Adv. Polym. Technol. (2018), https://doi.org/10.1002/adv.21850.
[59] D. Kumar, J.P. Gittings, I.G. Turner, C.R. Bowen, A. Bastida-Hidalgo, S.H. Cartmell, Polarization of hydroxyapatite: influence on osteoblast cell proliferation, Acta Biomater. 6 (2010) 1549–1554, https://doi.org/10.1016/j.actbio.2009.11.008.
[60] R. Xu, Effect of whey protein on the proliferation and differentiation of osteoblasts, J. Dairy Sci. 92 (7) (2009) 3014–3018, https://doi.org/10.3168/jds.2008-1702.
[61] Y.L. Chang, C.M. Stanford, J.S. Wefel, J.C. Keller, Osteoblastic cell attachment to hydroxyapatite-coated implant surfaces in vitro, Int. J. Oral Maxillofac. Implants. 14 (1999) 239–247, https://doi.org/10.5591/978-1-57735-516-8/IJCAI11-280.
[62] S.J. Gutiérrez-Prieto, S.J. Perdomo-Lara, J.M. Diaz-Peraza, L.G. Sequeda-Castañeda, Analysis of *In Vitro* osteoblast culture on scaffolds for future bone regeneration purposes in dentistry, Adv. Pharmacol. Sci. 2019 (2019) 5420752, https://doi.org/10.1155/2019/5420752.